Hippocampal morphology and cytoarchitecture in the 3D BigBrain

DeKraker, J.[1,2], Lau, J.C.[2,3,4], Ferko, K.M.[1,2], Khan, A.R.[2,4,5]*, Köhler, S.[1,6]*

[1]Brain and Mind Institute,
[2]Robarts Research Institute, Schulich School of Medicine and Dentistry,
[3]School of Biomedical Engineering,
[4]Dept Clinical Neurological Sciences, Division of Neurosurgery,
[5]Dept Medical Biophysics,
[6]Dept Psychology,
University of Western Ontario
*co-senior authorship

Abstract

The internal architecture of the hippocampus is challenging to map in detail using traditional histology and in-vivo neuroimaging. This is due, in part, to its complex archicortical folding that is difficult to appreciate in both modalities. Here, we aimed to overcome this challenge by leveraging the unique histological dataset available as open-source 3D BigBrain. Specifically, we investigated the relationship between topology, laminar cytoarchitecture, and detailed morphology with respect to hippocampal subfields and its anterior-posterior axis. Inspired by computational parcellation methods used in the neocortex, we topologically 'unfolded' the hippocampus and mapped it with respect to 5 morphological and 10 laminar features. Several features, including thickness, gyrification, and mean neuronal density, clearly differed between subfields. Indeed, data-driven clustering of all features revealed subdivisions which closely resemble manually defined subfields. Some features, most notably gyrification, also showed anterior-posterior differences within subfields, which may relate to connectivity and functional differences described in previous literature. Overall these findings offer quantifiable markers of hippocampal subfields, and provide new anatomical insight into the topology and properties of hippocampal tissue. Future applications could involve translation to in-vivo MRI for probing the internal hippocampal architecture at this mesoscale in cognition and disease.

Keywords

Hippocampal subfields, Cortical folding, Laminar, Morphology, Neuroimaging

1. Introduction

The hippocampus is one of the most heavily investigated brain structures in neuroscience. Much research in recent years has focused on questions about its subdivisions, guided by the idea that different regions within the hippocampus may perform different functions and may also be differentially prone to disease (Small, Schobel, Buxton, Witter, & Barnes, 2011). These developments pose central question as to how to characterize subdivisions in anatomical terms. Traditionally, most proposed subdivisions have relied on histology and cytoarchitecture, leading to the notion of distinct hippocampal subfields that typically include the the subicular complex, Cornu Ammonis 1 to 4, and the dentate gyrus (Duvernoy, Cattin, & Risold, 2013 for review). More recently, increasing interest has also emerged concerning graded differences along the anterior-posterior axis based on subfield composition and connectivity (Plachti et al., 2019; Poppenk, Evensmoen, Moscovitch, & Nadel, 2013; Strange, Witter, Lein, & Moser, 2014). An organizational principle that shapes these dimensions, i.e., subfields and anterior-posterior gradients, is the complex topology within the hippocampus that results from its ontological development (DeKraker, Ferko, Lau, Köhler, & Khan, 2018; Duvernoy et al., 2013). This principle has received only limited investigation to date but requires careful consideration in any effort to characterize the internal architecture of the hippocampus. The current paper aims to investigate the relationship between hippocampal topology, morphology, and cytoarchitecture in humans, taking advantage of the unique and powerful “Big Brain” dataset that provides continuous histological sampling with full 3D coverage (K. Amunts et al., 2013). A particular promise of this approach lies in its applicability to in-vivo Magnetic Resonance Imaging (MRI).

While commonly used MRI measures do not allow for cytoarchitectural characterization, MR-based protocols have been developed to indirectly infer the locations of hippocampal subfields in humans based either on manually delineated landmarks or corresponding probabilistic atlases that are informed by histological reference material (Iglesias et al., 2015; Yushkevich, Amaral, et al., 2015; Yushkevich, Pluta, et al., 2015). However, traditional histological references can be problematic for several reasons. First, they often contain only select coronal slices taken from regions where folding is simplest, most frequently from the hippocampal body (Ding & Van Hoesen, 2015). Second, even in the hippocampal body slices are taken sparsely, limiting the amount of contextual features that can be gathered from neighboring slices or other planes of view. Third, histological preparation often deforms the tissue of interest relative to its in-vivo state, which is a problem for MRI co-registration unless the histological sample is also imaged prior to histological preparation. Finally, even among neuroanatomists there is some disagreement as to exactly which labels, stains, and histological features should be used for defining hippocampal subfields (see Wisse et al., 2017). Some previous studies have made use of ex-vivo MRI to aid in the translation of histology to MRI (Iglesias et al., 2015; Yushkevich et al., 2009) in an effort to mitigate some of these issues. However, even with such an approach, inter-individual differences in hippocampal morphology can impose limitations for inferring subfields or other structural features, when hippocampal topology is not considered.

It is well established that the human hippocampus is a folded component of archicortex that is continuous with the neocortex (as summarized, for example, by Duvernoy et al., 2013; Nieuwenhuys, Voogd, & van Huijzen, 2013). The hippocampal folds include wrapping around its

innermost region - the dentate gyrus, as well as anterior-posterior folding that is sometimes referred to as dentation, digitation, or gyrification. The gyrification seen in the hippocampus is morphologically similar to gyrification in the neocortex (although not necessarily based on the same ontogeny). It has been shown to vary considerably between individuals (Chang et al., 2018; DeKraker et al., 2018) and can be affected by disease, such as temporal-lobe epilepsy (Blümcke et al., 2013). This folding is an important aspect of understanding the internal structure of the hippocampus, and for appreciation of the continuity of subfields, particularly in its anterior portion that includes the uncus (Ding & Van Hoesen, 2015). Topological analyses can provide a framework for extracting these continuities, for example through unfolding (DeKraker et al., 2018), and offer the basis for laminar and further morphological characterization of complete hippocampal structure in 3D, including subject-specific gyrification.

The dataset made publicly available by BigBrain (K. Amunts et al., 2013) provides a unique opportunity to conduct topological analyses of histology data in 3D, and to examine topological measures in unfolded tissue. This dataset consists of 3D histology, digitally reconstructed from images of a serially sectioned and stained healthy cadaveric brain. Waehnert recently showed that the dataset can be used for 3D characterization of specific laminar features in neocortex that takes gyrification into account (Waehnert et al., 2014). In the current project, we used reconstructed blocks of the left and right hippocampi (40um isotropic) to identify topologically-derived laminar and morphological features under our unfolded hippocampal framework. To characterize laminae, we focused on 10 computationally derived features describing the distributions of neurons (Katrin Amunts et al., 1999). Morphological features were also computationally derived and included thickness, curvature, inner and outer surface textures, as well as gyrification. We then compared these morphological and laminar features to classic descriptions of subfields and examined variations along the anterior-posterior hippocampal axis. We anticipated that the features examined would differ substantially between subfields. Therefore, we also tested whether a data-driven feature-based approach to subfield segmentation would yield similar results as manual subfield segmentation. This type of approach is desirable for is objectivity and for its potential towards automating anatomical hippocampal characterization.

2. Materials and Methods

The backbone of our analyses was to impose a topological unfolding framework to manual hippocampal traces, a method that we previously developed for 7T MRI (DeKraker et al., 2018). We then extracted various morphological features of hippocampal structure from the left and right 3D BigBrain hippocampi. We computed laminar features based on the work of Katrin Amunts et al. (1999) with correction as in (Waehnert et al., 2014). We then performed unsupervised, data-driven clustering of these features and compared resulting clusters to manually segmented hippocampal subfields. Finally, we examined anterior-posterior differences in hippocampal structure.

2.1 Materials

Histological data used in this study came from the BigBrain dataset bilateral 40um^3 resolution hippocampal blocks stained for neuronal cell bodies (ftp://bigbrain.loris.ca/BigBrainRelease.2015/3D_ROIs/Hippocampus/) in addition to serial

section images before 3D reconstruction at 20um^2 resolution (ftp://bigbrain.loris.ca/BigBrainRelease.2015/2D_Final_Sections/Coronal/Png/Full_Resolution/) (K. Amunts et al., 2013). Because of the large file sizes, tracing and application of our unfolding framework were performed on downsampled images (80um isotropic) before upsampling by nearest-neighbour interpolation in the case of labelmaps and linear interpolation in the case of unfolding solutions.

2.2 Manual Tracing

Detailed histological tracing was performed for each hippocampus by a combination of manual tracing and the user-guided computational tools in ITK-SNAP 3.6 (Yushkevich et al., 2006). A general label for hippocampal grey matter (subiculum and CA1-4) was traced first, and this tissue was later manually divided into subfields. The dentate gyrus (DG) was given a separate label as it is topologically disconnected from the rest of the archicortex, but was easily distinguishable by its very high granule cell density. Only the laminae which contained stained neuronal cell bodies - stratum pyramidale, oriens, and lucidum - were traced (Figure 1). Stratum radiatum, moleculare, and lacunosum (SRLM) and the alveus were not traced even though they are sometimes considered laminae of the archicortex containing dendrites and axons of pyramidal cells (Duvernoy et al., 2013), because they were not stained by this contrast (though note that some of these strata contain interneurons - see Supplementary Materials section A for discussion).

Subfields segmentation (i.e. the division of archicortical grey matter into distinct subfields) was performed in 3D by rater KF according to the criteria outlined by Ding & Van Hoesen (2015). To maximally utilize the histological features available in BigBrain, original 20um images were also consulted every 2mm in order to make use of the highest resolution available. These segmentations included the subiculum and CA1-4, but did not differentiate the regions within the subicular complex due to lack of resolution and since no myelin staining was available. Subfields were traced through the entire length of the hippocampus including the uncus and vertical component of the uncus, in which Ding & Van Hoesen (2015) describe modified versions of the same subfields. Because the vertical component of the uncus is very thin, the subfields there were not easily discriminable and so they were partially inferred from neighbouring regions of the hippocampus. All borders were then smoothed by morphological closing and opening to remove small border discrepancies between neighbouring slices.

Structures surrounding the hippocampus were traced only in the regions that border the hippocampus. These labels included medial-temporal lobe neocortex (MTLc) (entorhinal and parahippocampal regions), hippocampal-amygdalar transition area (HATA), and indusium griseum (ind. gris.). HATA borders were clearly discriminable from archicortex by a marked change in density and physical separation from archicortical neurons. Ind. gris. and MTLc borders were less clear, and so they were demarcated using the heuristics used in previous work in MRI. See Supplementary Materials section A for further discussion of these structures.

2.3 Topological unfolding framework

In previous work (DeKraker et al., 2018), we imposed a topological unfolding framework on the hippocampus by solving Laplace's equation over the domain of the hippocampus under multiple sets of boundary conditions: anterior-posterior, proximal-distal, and laminar. The

anterior-posterior and proximal-distal solutions can then be used to index regions of the hippocampus in 2D according to its topology, irrespective of inter-individual differences in gyrifications, rotation, curvature, size, orientation, or position of the hippocampus. This provides implicit registration between hippocampi despite inherently different morphologies. We applied the same approach to the current hippocampal traces (see Figure 2 for illustration). However, note that several minor improvements were made to this code which are detailed in Supplementary Materials section B.

Waehnert et al. noted that neocortical laminae are displaced due to curvature in gyri and sulci, and they propose an 'Equivolume' model that captures this feature better than a Laplacian (or equipotential) solution (Waehnert et al., 2014). Their model is motivated by the observation that a given lamina, for example near the pial surface, will stretch at the apex of a gyrus and compress at the depth of a sulcus, causing it to become thinner and thicker in these respective regions and vice versa for laminae at the white matter surface. Thus, we also included an alternative laminar indexing system using the Equivolume model solution obtained from Nighres (Landman et al., 2013). Again, this was performed on the downsampled (80um) traces before upsampling as above. The resulting model had fewer gyrification-related artifacts in laminar profiles so was used for all subsequent laminar analyses. However, some other artifacts were observed under this model solution, likely as a result of the rough texture of the subiculum surface (see Supplementary Materials section C for details).

2.4 Morphological feature extraction

Each morphological feature is illustrated in the top left panel of Figure 3. Thickness estimates were obtained across the unfolded space of the hippocampus as in previous work, that is, by generating and measuring streamlines in 3D across the laminar Laplacian solution obtained from our topological unfolding framework. Curvature estimates were obtained by generating a mid-surface along the hippocampus with the vertices being interpolated xyz coordinates from each unfolded point at a laminar distance of 0.5, which is the midpoint between the inner and outer surface. Smoothing of face normals was applied, and mean curvature was then estimated at each vertex (see Supplementary Materials section B for details). The inner (i.e. adjacent to the SRLM; continuous with the neocortical pial surface) and outer (i.e. adjacent to the alveus, continuous with the neocortical white matter surface) surfaces of the hippocampus were rougher than their mid-surface counterpart due to other features such as subicular 'islands' of cell bodies shown in Figure 1. We thus additionally computed curvatures of these surfaces after smoothing as above. Gyrification is typically defined as a ratio outer surface area, for example that of a brain mask over gyrified surface area, in this example including sulcal area (Larsen, Nielsen, & Sporring, 2006). Since the hippocampus is an open-ended cortical surface it does not map easily to an outer surface area or to a sphere as in the neocortex, and so our unfolding framework instead maps it to a rectangle. We thus defined gyrification as a ratio of native space surface area over unfolded surface area at each unfolded point.

2.5 Laminar feature extraction

We extracted laminar profiles along the Equivolume laminar solution (see Methods section 2.3), and then summarized these profiles using the same 10 features consistently used by Katrin Amunts et al. (1999). Briefly, this involved sampling staining intensities (y) along a laminar profile through the cortex, and calculating the mean (Mean(y)). This intensity profile was

then treated as a distribution (x), and the mean (Mean(x)) and first 3 moments (SD(x), Skew(x), and Kurt(x)) were calculated. The absolute value of the derivative (Abs.Deriv) of the profile was then calculated (y→y.d), and the same measures (e.g. Mean(y.d), Mean(x.d), etc) were calculated. These methods are illustrated with corresponding terminology at the top of Figure 3.

There were several methods developed for 3D MRI which we were able to incorporate into this analysis and other differences from the analyses performed by Katrin Amunts et al. (1999). Firstly, we sampled laminar profiles under the 3D Equivolume model that minimizes distortions in laminae due to curvature (see Methods section 2.4). Secondly, our laminar sampling was not as dense because of the reduced resolution available in the current data and the fact that the laminae of the archicortex are generally thinner than neocortex. Lastly, we included only laminae containing neuronal cell bodies (see Methods section 2.2). Further details on these differences between our Methods and those of Amunts et al. (1999) can be found in Supplementary Materials section B.

2.6 Data-driven segmentation

In order to cluster visually-homologous regions of the feature maps into segments, we applied a scale-space representation employing image pyramids. That is, for each of the features extracted, we smoothed the data in unfolded space with a Gaussian kernel and a Laplacian of Gaussian kernel of sizes sigma=[2,4,8,16,32,64] in order to capture features at various spatial scales. The anterior 10% and posterior 10% of each feature was discarded due to high noise.

All morphological and laminar features from the left and right hippocampi were then reshaped into single vectors, z-scored, and then principal components analysis (PCA) was performed. K-means clustering was then computed on the first 7 components, which explained >1% variance each, with a fixed number of output clusters of k=5 (since manual segmentations contained 5 subfield labels). PCA followed by K-means clustering was ideal for this type of analysis for several reasons: 1) co-linearity among features can be clearly assessed using PCA prior to k-means clustering, 2) clusters were expected to be of comparable sizes, which k-means is biased towards, and 3) the number of clusters is knows a-priori. Clusters were then assigned subfield labels based on highest overlap. Dice overlap scores were calculated (Dice, 1945; Sørensen, 1948) in unfolded space for each subfield (i.e. disregarding thickness), excluding the 10% anterior and posterior edges that were removed due to high noise. We also explored clustering under k=[2,4,8,16,32] in order to determine the consistency of subfield or sensitivity to further subdivisions in the data, which is shown in Supplementary Materials section D. PCA variance explained per component, component loadings and visualization of the first 7 components can be viewed in Figure 5, along with the correlation between each feature.

2.7 Anterior-posterior variance

One hypothesis that we had based on prior literature was that there may be anterior-posterior differences in some aspects of hippocampal structure. We thus plotted select features of interest across the anterior-posterior axis within each subfield. All features can be seen in a Supplementary Materials section A, where we additionally fit linear trends to the data to determine whether anterior-posterior gradients were present in any subfield. In Results section 3.6 we focus only on the features mean neuronal density thickness, gyrification, and (Mean(y)) which most clearly differed between subfields and are of immediate interest in MRI.

3. Results:

3.1 Manual Tracing

Figure 1 shows BigBrain coronal slices alongside manually segmented subfields in the head, body, and tail of the hippocampus, as well as corresponding 3D models. Several features were detected in tracings of the hippocampus in 3D BigBrain that were not detected in previous in-vivo MRI work that we know of. Clusters of pyramidal cells or 'islands' can be seen on the inner surface of the subiculum (stratum lacunosum), which have been observed in histology throughout the presubiculum (Ding & Van Hoesen, 2015; Duvernoy et al., 2013 and others). A medial and anterior fold along the vertical component of the uncus, approximately 0.3mm thick and up to 3.6mm in length, was observed, as described in (Ding & Van Hoesen, 2015; Duvernoy et al., 2013). Finally, numerous gyrifications throughout the posterior body and tail of the hippocampus were observed, which was also observed using MRI in (Chang et al., 2018), though not to the extent seen here. This was most prominent in CA1, but was also present in the DG and in CA4 which followed the same gyrification scheme as CA1. Models of the dentate gyrus alone and additional anatomical notes can be found in Supplementary Materials section A. Total volumes of each subfield can be seen in Table 1. Note that these volumes are smaller than what is typically reported in MRI, which may be due to our exclusion of alveus and SRLM laminae which can be hard to differentiate from partial voluming in MRI, but may also be influenced by tissue shrinkage during histological processing.

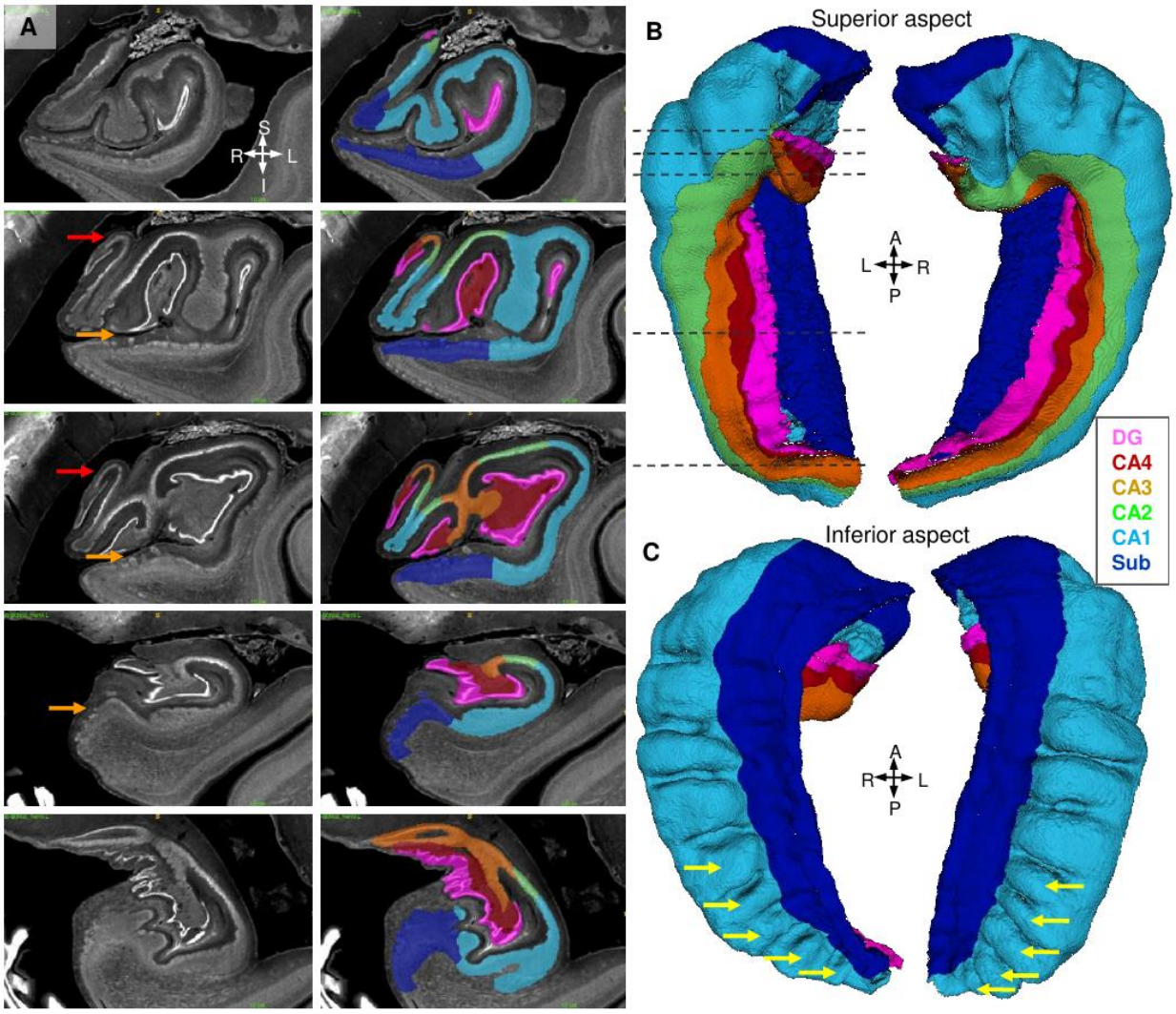

Figure 1. Manual traces of hippocampal archicortex and segmentation into subfields. A) shows coronal slices through the left hippocampal head (rows 1-3) body (row 4) and tail (row 5), with manual segmentations overlaid in the images to the right. B) shows 3D models of each hippocampus as seen from their superior aspect, with the inferior aspect shown in C). Dotted lines in B) indicate approximate locations of each coronal slice shown in A). SRLM, vestigial hippocampal sulcus, alveus, and fimbria were excluded from all labels. Red arrows indicate anterior folding in the vertical component of the uncus, orange arrows indicate 'islands' of neuronal cell bodies in the subicular stratum lacunosum, and yellow arrows indicate gyrifications in the posterior body and tail of the hippocampus.

Table 1. Volumes of each manually defined subfield (mm^3).

	Left	**Right**
Sub	345.9	282.5
CA1	574.0	534.0
CA2	46.6	40.6
CA3	66.9	54.4
CA4	109.0	107.4
DG	140.1	131.1

3.2 Topological unfolding

Figure 2A shows the proximal-distal and anterior-posterior Laplacian solutions which make up the two axes of our topological unfolded space. Figure 2B shows a mid-surface mesh of the hippocampus, coloured according to manually segmented subfields as in Figure 1. This surface was then mapped to 2D unfolded space according to the anterior-posterior and proximal-distal Laplace solutions. In unfolded space, subfields are relatively constant from anterior to posterior, with subiculum being proportionally larger in the very anterior and smaller in the very posterior, however these may be artefacts of manual segmentation since these region are very small in native space.

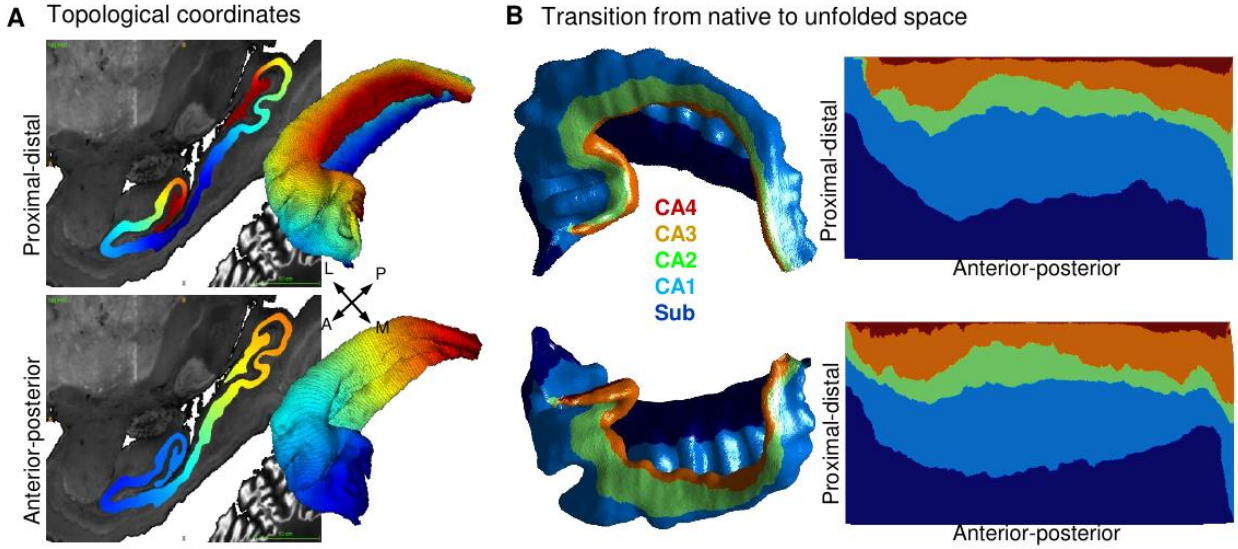

Figure 2. Topological unfolding framework in 3D BigBrain with hippocampal subfields. A) Sagittal slice and 3D models of the Laplacian solutions (proximal-distal and anterior-posterior) for the right hippocampus. B) Mid-surface topological models of the left and right hippocampi in native and unfolded space.

3.3 Characterization of the hippocampus in unfolded space

Figure 3 shows a full characterization of the left and right BigBrain hippocampi with respect to the 5 morphological and 10 laminar features described in Methods sections 2.4 and 2.5. These methods are illustrated at the top of the figure. As in related work (DeKraker et al., 2018; Duvernoy et al., 2013), thickness was highest in the subiculum and CA4 and lowest in CA2. Curvature was generally high in subiculum, which reflects its outward curling away from the rest of the hippocampus, but in CA1 vertical bands of positive and negative values can be seen which correspond to the hippocampal gyrifications seen in Figure 1. This region is also highlighted by our gyrification measure, which differs from curvature in that it does not vary by direction. Inner surface texture shows an almost honeycomb texture that is most prominent in the subiculum where subicular ‘islands’ of neurons are found in stratum lacunosum (Duvernoy et al., 2013). Outer surface texture appears smoother, and more closely resembles the mid-surface curvature measure. Note that the surface textures measures differ from the curvature measure only in that they capture very local details. Thus, they may not be available in lower resolution data. Thus features such as thickness and gyrification may be especially of interest in translation of this work to MRI, particularly because they show such clear distinction between subfields.

Of the laminar features computed here, Mean(y) was highest in region CA2, which also agrees with the high neuronal densities observed in this region (Duvernoy et al., 2013). Mean(x) showed almost the inverse pattern, with high values in all regions except CA2. This means that the distribution of neurons was shifted towards the inner surface in CA2. SD(x) was highest in CA2, indicating a wide distribution of neurons relative to the thickness of that tissue. This was counter-intuitive since in native space CA2 appears to have a tight distribution of neurons, however, relative to its small thickness the distribution is wide. The fact that the SD(x) and thickness features differ so drastically, despite our intuition from native space images that they should be similarly small in CA2. The remaining 7 laminar features become more complex and quite similar to Mean(y), Mean(x) or SD(x). Thus some of these features may be redundant but we nevertheless included them for consistency with previous work in the neocortex (Katrin Amunts et al., 1999).

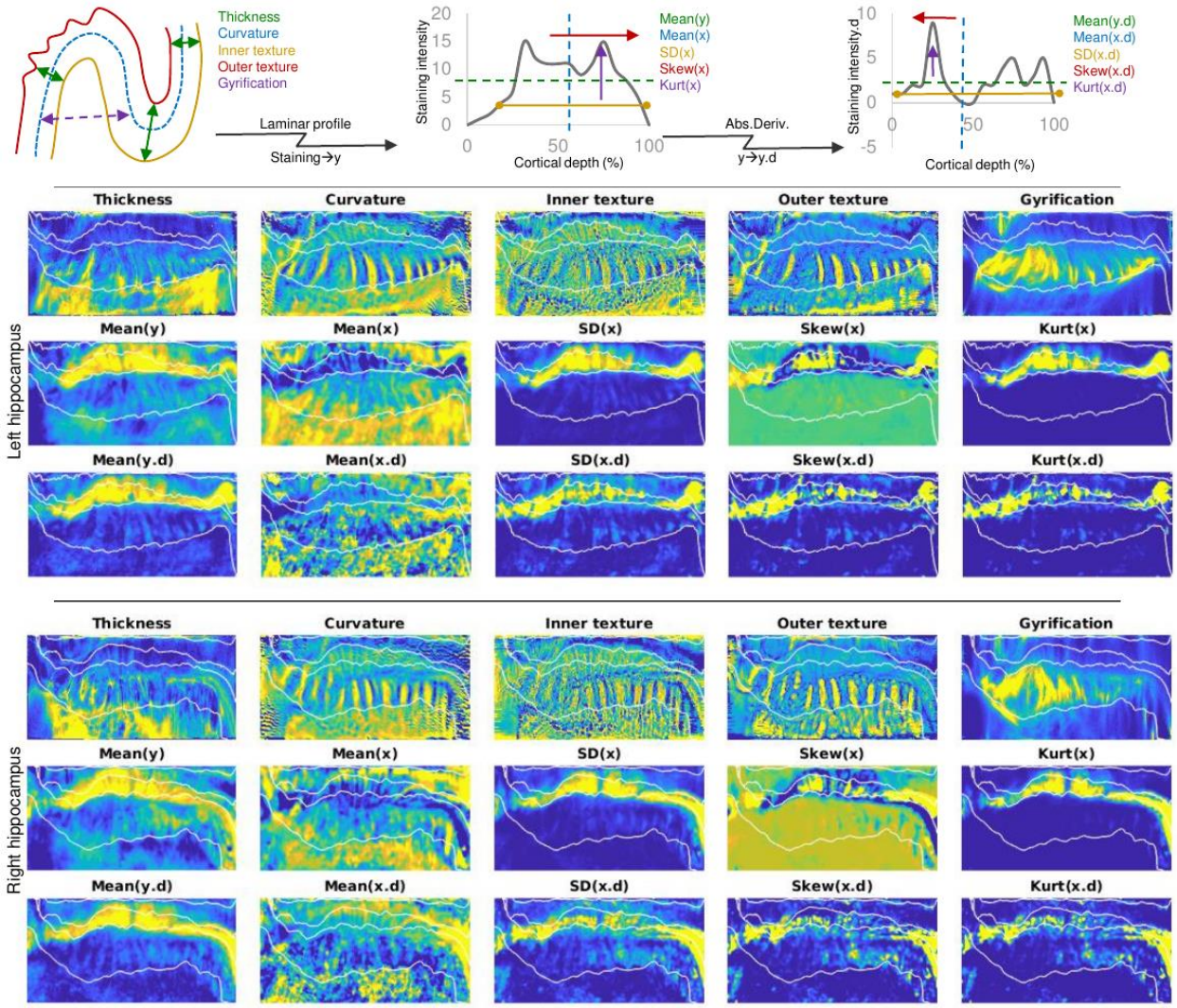

Figure 3. Characterization of the hippocampus using morphological and laminar features. The top diagrams illustrate how each feature is derived (see Methods section 2.4 and 2.5 for details). Top left shows an example segment of cortex, while the top centre and top right show an example laminar profile and its absolute derivative (Abs.Deriv), respectively (Katrin Amunts et al., 1999). Heat maps below show the z-scored values of each feature across the unfolded hippocampus in the left and right hemispheres. Overlaid in white are manually defined subfield borders.

3.4 Data-driven clustering resembles hippocampal subfields

Many of the features in figure 3 show show a clear distinction between the different manually defined subfields, and so we sought to determine whether a combination of these features could be used to independently derive some or all of the subfield boundaries. Figure 4 shows the results of data-driven clustering of the above features using a Gaussian image processing pyramid to capture multiple spatial scales, PCA to group features into orthogonal sets, and k-means clustering (Methods section 2.6). We compared clusters to their closest corresponding manually defined subfield using Dice overlap scores in Table 2 and found good (0.7) to very good (0.8+) overlap was seen for most subfields. Manually defined region CA2 had two data-driven clusters that overlapped with it (orange and green in Figure 4). The green cluster corresponded to the most dense regions of CA2 (e.g. where Mean(y) and SD(x) were high), and several other laminar features echoed this pattern. The fact that multiple features echoed this pattern may have contributed to why two clusters were generated in CA2 rather than just one. That is, the variance within CA2 may have been amplified by the presence of redundant features. When both the orange and green clusters were combined, they overestimated the total size of CA2 and impeded on regions that were manually defined as CA3 and CA1. Subfield CA4 was never given a unique cluster and was instead included with CA1 or CA3. This remained true even when the number of clusters (k) was increased up to k=16 (Supplementary Materials section D). Overlap with CA3 is to be expected given their topological closeness, but overlap with CA1 may be because despite their topological separation, both of these regions were thicker and contained a lower density of neurons than the other CA fields. Finally, the current analyses did not reveal any evidence for the subregions of the subicular complex as described by Ding (2013), which would appear as horizontal bands at the proximal edge but no such bands were observed even with additional clusters (see Supplementary Materials section D).

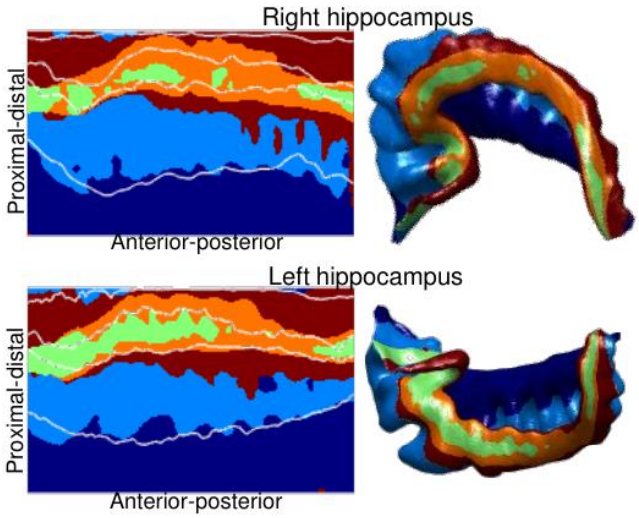

Figure 4. Data-driven k-means clusters of features. The left two images show k-means clusters in unfolded space with k=5, with manually defined subfield borders overlaid in white. The right two images show the same data in native space with 10% anterior and posterior edges extrapolated by nearest neighbour.

Table 2. Dice overlap scores between k-means clusters and their closest corresponding manually defined subfield.

	Left	**Right**

Sub	0.92	0.91
CA1	0.74	0.73
CA2	0.73	0.66
CA3	0.56	0.58
CA4	0	0

3.5 PCA breakdown

In order to better understand the inherent structure of the data used in the above k-means clustering, we examined various PCA metrics. Figure 5A shows the total variance explained by each PCA component, and only the first 7 components explained >1% of the variance and were included in subsequent analyses. Figure 5B and D show a breakdown of the first 7 principal components. The first and most prominent component was most highly correlated with most laminar features features, except Mean(x), Skew(x), and Mean(x.d) which showed an anti-correlation. Visualization of this component shows consistently high values in CA2. This makes sense that most laminar features showed uniquely high values in CA2, while Mean(x), Skew(x), and Mean(x.d) contained low values in this region. Subsequent components explain a decreasing portion of the total variance in the data, but correlate with different input features. Visual inspection of these components shows that some loosely follow the contours of the subfields. For example, component 3 quite clearly alternates low and high between subiculum, CA1, CA2, and CA3. Others, particularly components 5-7, appear to contain little subfield-related variance and may reflect noise captured by the later components. Interestingly, components 2 and 3 appear to show gradual anterior-posterior differences, with lower values in the anterior and higher in the posterior in component 2 and vice-versa in component 3.

Of the features used in this analysis, some were more correlated with each other than others (Figure 5C). In particular, all morphological features tended to be correlated with each other while all laminar features tended to be correlated or anti-correlated with each other, with only small correlations between morphological and laminar features. The fact that laminar features tended to be uncorrelated with morphological features is in line with the goal of the Equivolume model (Waehnert et al., 2014) which we applied in order to remove the effects of curvature on laminar displacement. Thus when modelled in 3D using the appropriate methods, morphological and laminar features represent apparently different levels of structural information about tissue within the hippocampus.

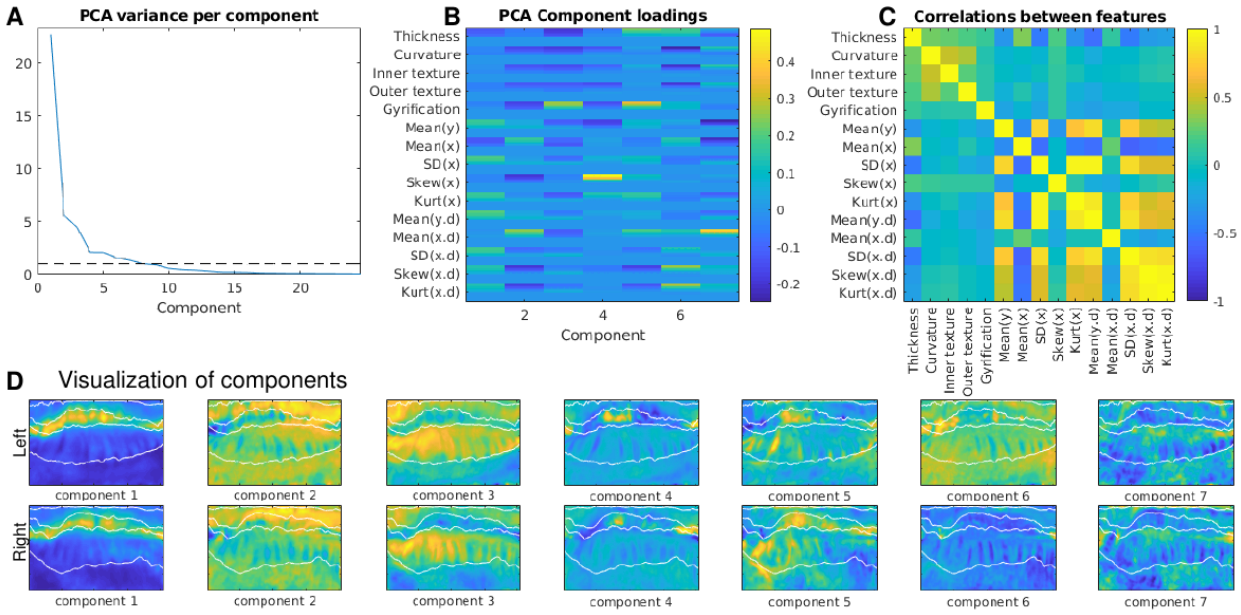

Figure 5. Exploration of inherent feature variance. A) shows PCA component loadings from each feature with a dotted line at 1% after which subsequent components were discarded. B) shows the loadings of the first 7 components on each feature, with multiple rows for the various smoothing kernels applied to each feature. C) shows the correlation between all features. D) shows a visualization of the first 7 components, with manually defined subfield borders overlaid in white.

3.6 Anterior-posterior variation

We aimed to determine whether any feature showed anterior-posterior differences across the hippocampus, as reported in other studies. We thus plot features of interest across only the anterior-posterior gradient to better visualize possible trends (Figure 6). We focused on the features gyrification, thickness, and mean neuronal density (Mean(y)) since these features showed high contrast between different subfields, but this data can also be viewed for all features in Supplementary Materials section A. Within each features a high degree of separation can be seen between some subfields. That is, CA4 and subiculum have high thicknesses, CA4 and CA1 have high gyrification, and CA2 and CA3 have high neuronal density relative to the other subfields. This was also noted in Results section 3.3. Thickness and gyrification tended to show lower values at the anterior and posterior extremes, or in the vertical component of the uncus and tail of the hippocampus, which was also observed during manual tracing (Results section 3.1). However in the remainder of the hippocampus, namely the head and body, thickness remained relatively constant in each subfield while gyrification gradually decreased, as observed during manual tracing. Neuronal density was notably lower in most subfields in the anterior, approximately corresponding to the vertical component of the uncus, but showed only minor fluctuations throughout the rest of the hippocampus.

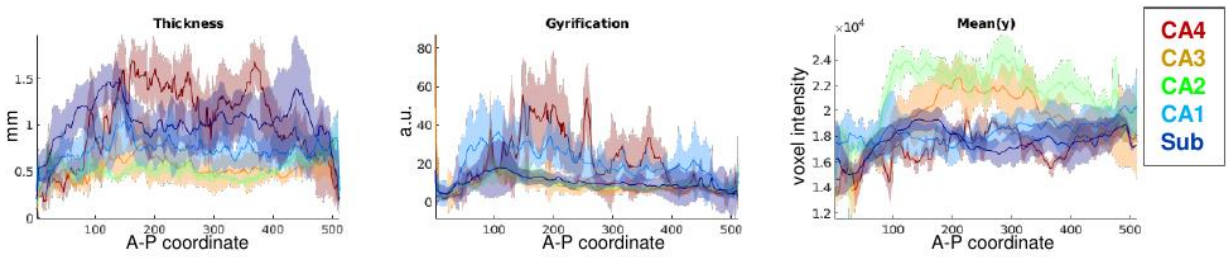

Figure 6. Features of interest plotted with respect to the anterior-posterior axis of the hippocampus. Colours indicate manually defined subfields, and shaded areas indicate standard deviation. Data are combined across the left and right hippocampi.

4. Discussion:

The current paper aimed to investigate the relationship between hippocampal topology, morphology, and cytoarchitecture with respect to hippocampal subfields and anterior-posterior gradients. We unfolded the hippocampus in the 3D BigBrain dataset and mapped computationally-derived morphological and laminar features in unfolded space, providing detailed and quantified maps of these features across the full extent of the hippocampus.

4.1 Subfield-related structural variance

Manual tracing and modelling of the hippocampus (Figure 1) at the level of resolution available in BigBrain revealed several features not seen in any 3D atlas that we are aware of. First, medial folding in the posterior end of the vertical component of the uncus was observed, similar to the inward 'curling' of the CA fields around the innermost DG in the rest of the hippocampus. Second, 'islands' of pyramidal neurons were present in stratum moleculare in the subiculum. Third, gyrifications were present throughout the head, body, and tail of the hippocampus but were most prominent in CA1. These gyrifications were also echoed in the underlying DG (where the term dentation is often used to refer to this feature) and region CA4 that the DG partially encircles. Each of these features has been described in histology (Ding & Van Hoesen, 2015; Duvernoy et al., 2013), but has not been reconstructed in a 3D model at this level of detail. For example, Adler et al. (2018) and Iglesias et al. (2015) both performed detailed and fully 3D segmentation of the hippocampus and its subfields using ex-vivo MRI data, with additional histological data in the same participants provided by Adler et al. Our approach extends beyond these studies by utilizing higher-resolution tracing and by using histological cues inherent in the same images. Furthermore, our manual traces and quantitative analyses fully respect the topology of the hippocampus and, in turn, the continuity of each subfield throughout the entire length of the hippocampus.

After applying our topological unfolding system, we computationally extracted morphological and laminar features from the hippocampus (Figure 3). Many of these features agree with qualitative descriptions by neuroanatomists, as discussed in Results section 3.3. Some of these features may be informative for in-vivo imaging as well. For example, measures of thickness and gyrification can be obtained under our topological unfolding framework given sufficiently detailed segmentations, regardless of the availability of cytoarchitectonic features. These two features in particular show good contrast between subfields Subiculum, CA1, and CA4, and so they could be explicitly leveraged to guide segmentation or registration to

histological reference materials in future MRI work. This may have been underappreciated in other in-vivo studies, including our own previous MRI study, where some of the gyrifications in the body and tail of the hippocampus could not be detected. This would lead to overinflated thickness measures, larger overall volumes, and perhaps differences in the proportional sizes of some subfields along the anterior-posterior extent of the hippocampus. Quantitative MR, such as T1 mapping, may also provide cues to approximate cytoarchitectonic features and indeed in our previous work we observed higher T1-weights in CA2 and CA3 (DeKraker et al., 2018) which may be driven by higher neuronal cell densities as observed in the current study. Thus we feel there is great promise in characterising or segmenting the hippocampus in future MRI work using the features described here.

We performed data-driven clustering of all features at various spatial scales to determine whether we could replicate the classically described hippocampal subfields using a completely data-driven approach. Results from clustering yielded generally high overlap with manual subfield segmentations in most cases (Table 2), with several exceptions that are outlined in Results section 3.4. One particularly interesting observation was that CA4 was consistently assigned the same cluster as CA3 or CA1, even though it shares no topological boundary with CA1. The shared structural elements between CA4 and CA1, particularly their relatively high thickness, gyrification, and low density of neurons, may relate to why certain diseases, such as subtypes of epilepsy, selectively affect CA1 and CA4 similarly (Blümcke et al., 2013; Duvernoy et al., 2013). Finally, the current analyses did not reveal any evidence for the subregions of the subicular complex as described by Ding (2013). This was not surprising for two reasons: 1) the scale of the subicular subregions is smaller than that of the other hippocampal subfields, and so the data or the methods here may not be sensitive enough to detect them, and 2) BigBrain only contains a single contrast (neuronal cell bodies), while other contrasts (particularly myelin) or even immunochemical profiles are often used to detect these subregions (Ding, 2013; Ding & Van Hoesen, 2015). Overall, while the subregions of the subiculum were not observed and region CA4 was not assigned a unique cluster, we found strong evidence that data-driven methods inherently divide the hippocampus into subiculum, CA1, CA2, and CA3 as in classical histology studies.

To further explore the inherent dimensionality of these structural features, we examined the principle components of all features (Figure 5). From this we noted that the most prominent components varied in such a way that followed the contours of some or all subfield borders (see Results section 3.5). This suggest that the inherent structural variance in the hippocampus most naturally follows a proximal-distal patterning as seen in the classic subfield definitions. Some components additionally hinted at inherent anterior-posterior differences across the hippocampus.

4.2 Anterior-posterior structural variance

Anterior-posterior structural differences in the hippocampus are particularly of interest given the growing body of literature suggesting functional anterior-posterior differences across the hippocampus (e.g. Plachti et al., 2019; Poppenk et al., 2013; Strange et al., 2014; Zeidman & Maguire, 2016). Structural anterior-posterior gradients are difficult to assess using conventional histology given that coronal or sagittal sections are typically out of plane with respect to the different subfields in most of the hippocampus. This highlights the utility of the

unique approach provided by the 3D BigBrain dataset. Figure 6 shows the features gyrification, thickness, and neuronal density across the anterior-posterior axis of the hippocampus. Most notable anterior-posterior differences included differences in most features at the very anterior and posterior extents of the hippocampus. Previous work by Ding & Van Hoesen (2015) described the anterior most region - the vertical component of the uncus - as containing modified subfields that were much thinner than their counterparts throughout the rest of the hippocampus, consistent with our observations. The posterior tail of the hippocampus has received relatively little attention however, and for this reason we define this hippocampal boundary using heuristics as in previous work (DeKraker et al., 2018), given that it can be difficult to differentiate hippocampal tail from more posterior structures such as the indusium griseum and post-rhinal cortices. Thus, it is possible that some of these structures were included in our hippocampal labels and, indeed, their transition appears to be gradual in the current dataset. Clearly, these regions would benefit from further anatomical characterization.

The gyrificaton feature was low in the anterior uncus, high in the remainder of the hippocampal head, and gradually decreased towards the posterior of the hippocampus, most notably in CA1. Qualitatively, we have seen similar trends in gyrification in our previous 7T MRI study (DeKraker et al., 2018) and in other work (Chang et al., 2018), though both of these studies are limited in their ability to detect small gyrifications (i.e. those detected in this study had peak-to-peak distances as low as 2mm). Biophysical models of the development of gyrification suggest a relationship between gyrus size and cortical thickness (Striedter, Srinivasan, & Monuki, 2015; Zilles, Palomero-Gallagher, & Amunts, 2013), but no systematic anterior-posterior differences in thickness were seen in the present data despite clear decreases in gyrification size towards the posterior. Other structures such as white matter might also constrain gyrification patterns (Striedter et al., 2015), which may additionally have consequences for functional properties of different gyri. For example, (Henderson & Robinson, 2014) examined gyrification and structural connectivity in the neocortex and found more unified or modular graph theoretical properties within gyri, as opposed to sulcal regions which were more diffusely connected or hub-like. Similarly, Plachti et al., (2019; see also Libby, Ekstrom, Ragland, & Ranganath, 2012) recently performed parcellation of the hippocampus according to its functional connectivity and observed divisions primarily along the anterior-posterior extent of the hippocampus rather than across subfields (though some proximal-distal clustering was also observed, as in the present study). This functional parcellation likely reflects differences in connectivity across the anterior-posterior extent of hippocampus, and may even relate to modular divisions of function within a given gyrus as proposed in the neocortex by Henderson & Robinson (2014). One final related consideration is that the size of gyrifications differing across the anterior-posterior extent of the hippocampus could also influence the horizontal propagation of theta waves that have been observed in the rodent hippocampus (Lubenov & Siapas, 2009). This could also lead to different functional properties across the anterior-posterior extent of the hippocampus. These proposed relationships between gyrification and structural or functional connectivity in the hippocampus should be systematically explored in in future work.

4.4 Data and resources made available

Alongside this publication we release our detailed manually defined hippocampus and surrounding structure traces, manual segmentation of these traces into subfields, data-driven

clustering results, topological unfolding framework, Equivolume laminar model solutions, and each of the unfolded morphological and laminar features computed here. In addition, we have also made all the code used in this project available via Open Science Framework (https://osf.io/x542s/) and, in the spirit of open and reproducible research, we welcome additional investigations of this rich dataset.

5. Conclusions:

In this project we have mapped the topological folds of the hippocampus in the 3D BigBrain dataset. We extracted a set of morphological and laminar features characterizing this tissue, and found that some features, most notably thickness, gyrification, and mean neuronal density, clearly differentiated the hippocampal subfields. We further show that data-driven clustering of all features is sufficient to derive the subfields without further neuroanatomical annotations. Some features, most notably gyrification, were shown to vary along the anterior-posterior axis within subfields, which can only be appreciated given both high resolution and 3D context. Overall these data highlight promising avenues for detecting clinically relevant or cognitively informative differences in internal hippocampal architecture.

Acknowledgements

This work is supported by a Canadian Institutes for Health Research Project Grant (CIHR Grant # 366062). J.D. is funded through a Natural Sciences and Engineering Research Council doctoral Canadian Graduate Scholarship (NSERC CGS-D). J.C.L is funded through the Western University Clinical Investigator Program accredited by the Royal College of Physicians and Surgeons of Canada and a Canadian Institutes of Health Research (CIHR) Frederick Banting and Charles Best Canada Graduate Scholarship Doctoral Award. K.M.F is funded through an Ontario Graduate Scholarship (OGS).

We would also like to thank Dr. Alan Evans, Dr. Katrin Amunts, and all contributors to project 3D BigBrain for developing and releasing this invaluable resource.

References

Adler, D. H., Wisse, L. E. M., Ittyerah, R., Pluta, J. B., Ding, S.-L., Xie, L., … Yushkevich, P. A. (2018). Characterizing the human hippocampus in aging and Alzheimer's disease using a computational atlas derived from ex vivo MRI and histology. *Proceedings of the National Academy of Sciences of the United States of America*, *115*(16), 4252–4257.

Amunts, K., Lepage, C., Borgeat, L., Mohlberg, H., Dickscheid, T., -E. Rousseau, M., … Evans, A. C. (2013). BigBrain: An Ultrahigh-Resolution 3D Human Brain Model. *Science*, *340*(6139), 1472–1475.

Amunts, K., Schleicher, A., B$\diamondsuit$rgel, U., Mohlberg, H., Uylings, H. B. M., & Zilles, K. (1999). Broca's region revisited: Cytoarchitecture and intersubject variability. *The Journal of Comparative Neurology*, *412*(2), 319–341.

Blümcke, I., Thom, M., Aronica, E., Armstrong, D. D., Bartolomei, F., Bernasconi, A., … Spreafico, R. (2013). International consensus classification of hippocampal sclerosis in temporal lobe epilepsy: a Task Force report from the ILAE Commission on Diagnostic Methods. *Epilepsia*, *54*(7), 1315–1329.

Chang, C., Huang, C., Zhou, N., Li, S. X., Ver Hoef, L., & Gao, Y. (2018). The bumps under the hippocampus. *Human Brain Mapping*, *39*(1), 472–490.

DeKraker, J., Ferko, K. M., Lau, J. C., Köhler, S., & Khan, A. R. (2018). Unfolding the hippocampus: An intrinsic coordinate system for subfield segmentations and quantitative mapping. *NeuroImage*, *167*, 408–418.

Dice, L. R. (1945). Measures of the Amount of Ecologic Association Between Species. *Ecology*, *26*(3), 297–302.

Ding, S.-L. (2013). Comparative anatomy of the prosubiculum, subiculum, presubiculum, postsubiculum, and parasubiculum in human, monkey, and rodent. *The Journal of Comparative Neurology*, *521*(18), 4145–4162.

Ding, S.-L., & Van Hoesen, G. W. (2015). Organization and Detailed Parcellation of Human Hippocampal Head and Body Regions Based on a Combined Analysis of Cyto- and Chemoarchitecture. *The Journal of Comparative Neurology*, *523*(15), 2233–2253.

Duvernoy, H. M., Cattin, F., & Risold, P.-Y. (2013). *The Human Hippocampus*.

Henderson, J. A., & Robinson, P. A. (2014). Relations between the geometry of cortical gyrification and white-matter network architecture. *Brain Connectivity*, *4*(2), 112–130.

Iglesias, J. E., Augustinack, J. C., Nguyen, K., Player, C. M., Player, A., Wright, M., … Alzheimer's Disease Neuroimaging Initiative. (2015). A computational atlas of the hippocampal formation using ex vivo, ultra-high resolution MRI: Application to adaptive segmentation of in vivo MRI. *NeuroImage*, *115*, 117–137.

Landman, B. A., Bogovic, J. A., Carass, A., Chen, M., Roy, S., Shiee, N., … Prince, J. L. (2013). System for integrated neuroimaging analysis and processing of structure. *Neuroinformatics*, *11*(1), 91–103.

Larsen, R., Nielsen, M., & Sporring, J. (2006). *Medical Image Computing and Computer-Assisted Intervention – MICCAI 2006: 9th International Conference, Copenhagen, Denmark, October 1-6, 2006, Proceedings*. Springer Science & Business Media.

Libby, L. A., Ekstrom, A. D., Ragland, J. D., & Ranganath, C. (2012). Differential connectivity of perirhinal and parahippocampal cortices within human hippocampal subregions revealed by high-resolution functional imaging. The Journal of Neuroscience: The Official Journal of the Society for Neuroscience, 32(19), 6550–6560.

Lubenov, E. V., & Siapas, A. G. (2009). Hippocampal theta oscillations are travelling waves. *Nature*, *459*(7246), 534–539.

Nieuwenhuys, R., Voogd, J., & van Huijzen, C. (2013). *The Human Central Nervous System: A Synopsis and Atlas*. Springer Science & Business Media.

Plachti, A., Eickhoff, S. B., Hoffstaedter, F., Patil, K. R., Laird, A. R., Fox, P. T., … Genon, S. (2019). Multimodal Parcellations and Extensive Behavioral Profiling Tackling the Hippocampus Gradient. *Cerebral Cortex* . https://doi.org/10.1093/cercor/bhy336

Poppenk, J., Evensmoen, H. R., Moscovitch, M., & Nadel, L. (2013). Long-axis specialization of the human hippocampus. *Trends in Cognitive Sciences*, *17*(5), 230–240.

Small, S. A., Schobel, S. A., Buxton, R. B., Witter, M. P., & Barnes, C. A. (2011). A pathophysiological framework of hippocampal dysfunction in ageing and disease. *Nature Reviews. Neuroscience*, *12*(10), 585–601.

Sørensen, T. (1948). *A Method of Establishing Groups of Equal Amplitude in Plant Sociology Based on*

Similarity of Species Content and Its Application to Analyses of the Vegetation on Danish Commons.

Strange, B. A., Witter, M. P., Lein, E. S., & Moser, E. I. (2014). Functional organization of the hippocampal longitudinal axis. *Nature Reviews. Neuroscience*, *15*(10), 655–669.

Striedter, G. F., Srinivasan, S., & Monuki, E. S. (2015). Cortical folding: when, where, how, and why? *Annual Review of Neuroscience*, *38*, 291–307.

Waehnert, M. D., Dinse, J., Weiss, M., Streicher, M. N., Waehnert, P., Geyer, S., … -L. Bazin, P. (2014). Anatomically motivated modeling of cortical laminae. *NeuroImage*, *93*, 210–220.

Wagstyl, K., Lepage, C., Bludau, S., Zilles, K., Fletcher, P. C., Amunts, K., & Evans, A. C. (2018). Mapping Cortical Laminar Structure in the 3D BigBrain. *Cerebral Cortex* , *28*(7), 2551–2562.

Wisse, L. E. M., Daugherty, A. M., Olsen, R. K., Berron, D., Carr, V. A., Stark, C. E. L., … Hippocampal Subfields Group. (2017). A harmonized segmentation protocol for hippocampal and parahippocampal subregions: Why do we need one and what are the key goals? *Hippocampus*, *27*(1), 3–11.

Yushkevich, P. A., Amaral, R. S. C., Augustinack, J. C., Bender, A. R., Bernstein, J. D., Boccardi, M., … Hippocampal Subfields Group (HSG). (2015). Quantitative comparison of 21 protocols for labeling hippocampal subfields and parahippocampal subregions in in vivo MRI: towards a harmonized segmentation protocol. *NeuroImage*, *111*, 526–541.

Yushkevich, P. A., Avants, B. B., Pluta, J., Das, S., Minkoff, D., Mechanic-Hamilton, D., … Detre, J. A. (2009). A high-resolution computational atlas of the human hippocampus from postmortem magnetic resonance imaging at 9.4 T. *NeuroImage*, *44*(2), 385–398.

Yushkevich, P. A., Piven, J., Hazlett, H. C., Smith, R. G., Ho, S., Gee, J. C., & Gerig, G. (2006). User-guided 3D active contour segmentation of anatomical structures: significantly improved efficiency and reliability. *NeuroImage*, *31*(3), 1116–1128.

Yushkevich, P. A., Pluta, J. B., Wang, H., Xie, L., Ding, S.-L., Gertje, E. C., … Wolk, D. A. (2015). Automated volumetry and regional thickness analysis of hippocampal subfields and medial temporal cortical structures in mild cognitive impairment. *Human Brain Mapping*, *36*(1), 258–287.

Zeidman, P., & Maguire, E. A. (2016). Anterior hippocampus: the anatomy of perception, imagination and episodic memory. *Nature Reviews. Neuroscience*, *17*(3), 173–182.

Zilles, K., Palomero-Gallagher, N., & Amunts, K. (2013). Development of cortical folding during evolution and ontogeny. *Trends in Neurosciences*, *36*(5), 275–284.